Hierarchical domain structures associated with oxygen octahedra tilting patterns in lead-free (Bi1/2Na1/2)TiO3

To cite this article before publication: Dongli Hu *et al* 2022 *Nanotechnology* in press https://doi.org/10.1088/1361-6528/aca030

Hierarchical domain structures associated with oxygen octahedra tilting patterns in lead-free $(Bi_{1/2}Na_{1/2})TiO_3$

Dongli Hu†, Zhongming Fan†, William Sawyer, Mitchell Henderson, Duan Luo, Xiaoming Liu, Hui Gu, Xiaoli Tan*, Jianguo Wen*

Dr. Dongli Hu, Duan Luo, Dr. Jianguo Wen*

Center for Nanoscale Materials, Argonne National Laboratory, Lemont, IL 60437, USA

Dr. Dongli Hu, Prof. Hui Gu

School of Materials Science and Engineering, Shanghai University, Shanghai 200444, China

Prof. William Sawyer, Mr. Mitchell Henderson

Physics department, West Chester University of Pennsylvania, West Chester, PA 19383, USA

Dr. Zhongming Fan, Dr. Xiaoming Liu, Prof. Xiaoli Tan*

Department of Materials Science and Engineering, Iowa State University, Ames, IA 50011, USA

Abstract

Hierarchical domain structures associated with oxygen octahedra tilting patterns were observed in lead-free $(Bi_{1/2}Na_{1/2})TiO_3$ ceramics using aberration-corrected high-resolution transmission electron microscopy (HRTEM). Three types of domains are induced by distinct mechanisms: the "orientation-domain" is induced at micrometer scale formed by different tilting orientations of the oxygen octahedra, the "meso-chemical-domain" occurs at a few tens of nanometer scale by chemical composition variation on the A-site in the ABO_3 perovskite structure, and the "nano-cluster-region" runs across several unit-cells with apparent A-site cation segregation with oxygen vacancies clustering around Na cations. Based on HRTEM amplitude contrast imaging (ACI), the correlation between the oxygen octahedral tilting pattern and compositional non-stoichiometry was established. The role of the hierarchical domain structure associated with the tilting patterns of the oxygen octahedra on the ferroelectric behavior of $(Bi_{1/2}Na_{1/2})TiO_3$ is also discussed.

1. Introduction

$(Bi_{1/2}Na_{1/2})TiO_3$ (BNT) based lead-free compounds are promising materials to replace the lead-containing $Pb(Zr_{1-x}Ti_x)O_3$ in piezoelectric technologies in the future.[1] Although previous research has largely focused on BNT solid solutions with $BaTiO_3$, $SrTiO_3$, and $(Bi_{1/2}K_{1/2})TiO_3$ due to their outstanding electromechanical properties,[2–4] the detailed study on the BNT-based compound is of fundamental interest as it is an ideal model perovskite crystal with rich physics and chemistry involving cation displacement, oxygen octahedra tilting and A-site cation disorder.

The crystallographic and compositional complexity in BNT engenders the elucidation of its microstructure, even at room temperature, rather difficult. Jones *et al.* determined the space group at room temperature to be *R3c* which features the oxygen octahedral tilting about the three-fold axis (Glazer notation: $a^-a^-a^-$).[5] Gorfman *et al.* assigned a monoclinic (*Cc*) space group with the $a^-a^-c^-$ tilting pattern to the room temperature structure based on their high resolution single crystal x-ray diffraction results,[6] which was later supported by a systematic electron diffraction investigation conducted by Ma *et al*.[7] However, either *R3c* or *Cc* was then realized to be merely the average symmetry and the long-range crystal structure is found to be perturbed by various local deviations. First, an anti-phase boundary (APB) forms when two regions with the same tilting pattern but nucleated out of phase meet in the middle.[8,9] Second, the ferroelectric domain wall is the most common symmetry-breaking defect in ferroelectric crystals. Adjacent to a $\{110\}_c$ wall between two *R3c* domains, two oxygen octahedron layers on each side exhibit an $a^-a^-c^+$ tilting pattern, which can be regarded as an orthorhombic *Pnma* phase accommodating the local strain field.[10,11] Third, a little residual of the high temperature phase (tetragonal *P4bm*) persists at room temperature in the form of $(001)_c$ textured platelets, giving rise to the diffuse ½{*ooe*} type superlattice spots that are elongated along $<100>_c$ direction in the electron diffraction pattern.[9,12]

Domain structures in lead-free perovskite at an atomic scale has been extensively studied before as reported in references.[13–18] It should be noted that none of the aforementioned types of local deviation from the average symmetry has been found composition-related, such as A-site non-stoichiometry or A-site cation ordering.[19,20] Indeed, such correlation is uneasy to establish because those structures with extremely short coherent length can by no means be examined using conventional diffraction methods. In this paper, we employed the aberration-corrected high-resolution transmission electron microscopy (HRTEM) to identify orientation-associated domain in BNT ceramics. Moreover, the amplitude contrast imaging (ACI) mode in HRTEM enabled us to establish a clear correlation between the A-site non-stoichiometry and oxygen octahedra tilting patterns within the orientation-domains.

2. Experimental

Polycrystalline ceramic of $(Bi_{1/2}Na_{1/2})TiO_3$ was fabricated via the solid state reaction method. Powders of Na_2CO_3 (≥99.9 wt.%), Bi_2O_3 (≥99.9 wt.%), and TiO_2 (≥99.99 wt.%) were used as starting raw materials. The powders were mixed in ethanol according to stoichiometry and milled for 7 hours on a vibratory mill. After drying, the mixture was calcined twice at 850 °C for 3 hours, and then sintered at 1175 °C for 3 hours.

For the TEM specimen preparation, as-sintered ceramic pellets were mechanically ground and polished down to 120 μm thickness, and then ultrasonically cut into disks with a diameter of 3 mm. After mechanical dimpling and polishing, the disks were annealed at 250 °C for 2 hours and Ar-ion milled to the point of electron transparency. TEM observations were carried out using the Argonne Chromatic Aberration-corrected TEM (ACAT) operated at 200 kV. The ACAT microscope is equipped with an image corrector to correct both spherical and chromatic aberrations,

enabling information limit better than 0.08 nm at 200 kV. Detailed experimental setup can be found in Figure S1 in Supplementary Information and in our previous report.[21]

3. Results

3.1 Orientation-domains

The BNT ceramic is observed to have a typical grain size about 1 μm, as shown in Fig. 1a. The grain was tilted along the $<110>_c$ zone-axis, which allows studying the correlation between oxygen octahedra tilting pattern and A-site composition since the titanium column and the oxygen column are clearly separated when viewed along this direction.[22] The selected-area electron diffraction (SAED) pattern from the entire grain is shown in Fig. 1b. In this diffraction pattern, there is one set of extra diffraction spots compared with the $<110>_c$ SAED pattern of a cubic perovskite structure (similar to the diffraction pattern in Fig. 1c). Using one of these extra diffraction spots, for example, the $\frac{1}{2}[\bar{1}11]$ spot circled in Fig. 1b, a dark-field (DF) TEM image of the grain can be obtained (Fig. 1a). Several distinct domains are observed in this grain. The SAED pattern from a bright domain (highlighted with a green circle) is similar to Fig. 1b, but with slightly stronger intensity of $\frac{1}{2}\{111\}$ spots. A corresponding SAED pattern from the dark domain (highlighted with a red circle) exhibits the $<110>_c$ pattern without any extra $\frac{1}{2}\{111\}$ spots (Fig. 1c). Figure 1d and 1e show typical aberration-corrected HRTEM images taken from the two domains, respectively. The bright domain displays an alternatively up and down oxygen displacement pattern in TiO_2 planes marked with a green box (Fig. 1d); we termed this pattern "corrugated". On the other hand, the dark domain shows elongated oxygen columns perpendicular to TiO_2 planes marked by red ovals (Fig. 1e); we termed this pattern "split".

Given the fact that the $\frac{1}{2}\{111\}$ spots in the SAED pattern are essentially the $\frac{1}{2}\{ooo\}$ type superlattice diffraction originated from the oxygen octahedra tilting about the three-fold axis,[23] the different features observed from the two domains can be interpreted as the same tilting pattern

observed along two orthogonal directions, as illustrated in Fig. 1f. Assuming the oxygen octahedra are tilted about the $[\bar{1}11]_c$ direction, the projected image viewed along the $[\bar{1}10]_c$ direction (indicated by the green arrow in Fig. 1f) will produce a corrugated pattern (Fig. 1g). A projected image viewed along the perpendicular $[110]_c$ direction (indicated by the red arrow in Fig. 1f) will produce a split pattern (Fig. 1h). In our case where the entire grain is viewed along the $[\bar{1}10]_c$ direction, the region with the tilting axis oriented along $[\bar{1}11]_c$ appears as the corrugated domain, while the region with the $[111]_c$ tilting orientation forms the split domain. Simulated SAED patterns corresponding to corrugated and split patterns are shown in Fig. S2, matching with the experimental SAED patterns in Fig. 1b and 1c, respectively. Thus, the corrugated and split domains are, by their nature, "orientation-domains".

This conclusion is further confirmed by simulated HRTEM images using, for example, a structure reported in the reference.[24] The insets in Fig. 1d and 1e are simulated HRTEM images along $[12\bar{1}]$ and [110] of the R3C structure, respectively. In the "corrugated" region (Fig. 1d), the degree of corrugation is determined by the tilt angle of octahedra around the zone axis. In Fig. 1d, the tilt angle is directly measured as ~10º, consistent with the atomic model along this direction. In the "split" region (Fig. 1e), the oxygen columns are imaged as elongated dots due to the imaging resolution of the microscope (0.08 nm of the information limit) is larger than the projected distance between two split oxygen atoms. The oxygen elongation is not an artifact, since other atomic columns are imaged as round dots, for example, the titanium columns (circled in blue in Fig. 1e).

Similar to other types of domain boundary,[25] the orientation-domain boundary also has a special transitional structure. The HRTEM image shown in Fig. 2a was taken across an edge-on domain boundary shown in Fig. 1a. The left side of Fig. 2a has no corrugation but exhibits an elongation of the oxygen sites in a direction perpendicular to the TiO_2 plane. So, this portion of

the micrograph has the features characteristic of the split pattern described in Fig. 1e. The right side exhibits the up and down positions of oxygen atoms characteristic of the corrugated pattern illustrated in Fig. 1d. Moving from left to right, there is a general decrease in the elongation of the oxygen columns which leads to an ultimate disappearance on the right. Meanwhile, moving from right to left there is a general decrease in the degree of corrugation of the oxygen columns which leads to an ultimate disappearance on the left. In the boundary region, a combination of the split and corrugated patterns is evident, which is different from either the left or the right region of the micrograph. Figures 2b through 2d are zoomed-in HRTEM images from these three different regions in Fig. 2a, where Fig. 2c clearly shows the combined split-corrugated pattern. The boundary could be a sharp interface in the (100) or (010) planes, which is inclined to the observation direction. The observed transition from split to corrugated pattern is therefore due to the overlapping effect across the inclined boundary. However, we cannot rule out the possibility that the boundary is not sharp but resides in the plane of (001). Presumably, the domain boundary between the corrugated and split orientation-domains possesses elastic energy that needs to be accommodated. Unlike the ferroelectric domain boundary with a thin *Pnma* sheet reported previously,[12] the oxygen octahedra gradually adjust their tilting condition across the corrugated-split orientation domain boundary, forming a thicker transition layer.

3.2 Meso-chemical-domains

In addition to these orientation-domains, we found another level of domain structure associated with chemical composition variation, which we termed “meso-chemical-domains”. Such meso-domains, with a typical domain size of several tens of nanometers, can be found within orientation-domains as shown in elemental mapping using energy dispersive spectroscopy (Fig. S3). The composition of Ti and O columns maintain the same across the mapping area, but Bi and Na show compositional variation of about 10% from the line profile. This means the BNT ceramic is not

homogenous in terms of Bi and Na content at this length scale; there exists a deviation from the nominal chemical composition of 50% Bi + 50% Na on the A-site.

In order to better understand the oxygen octahedra tilting pattern within the meso-chemical-domain, we applied the newly developed amplitude contrast imaging (ACI) mode in HRTEM, which can not only discriminate between heavy and light element columns based on channeling contrast, but also enables us to explore the oxygen octahedra tilting patterns. For a TEM with a spherical aberration (C_s) image corrector, Urban and Jia *et al.* introduced the negative C_s imaging (NCSI) method to balance the contrast and resolution, which enables imaging all atomic columns including light elements such as oxygen.[26] Under the NCSI imaging mode, all atomic columns were imaged as white dots on a dark background; therefore, it is rather difficult to use this imaging condition to discriminate heavy and light elements. With the correction of both C_s and chromatic aberration (C_c), we are able to achieve ACI mode in HRTEM instead of phase-contrast HRTEM under conventional HRTEM and NCSI imaging modes.[21] Under the ACI mode, heavy elements columns show darker contrast compared to light elements due to the channeling contrast.[27] Figure 3a is a HRTEM image taken under the ACI mode from the corrugated domain in Fig. 1a. Note that it is more difficult to study the degree of split compared to the degree of corrugation. In this figure, we can see an obvious variation from bright to dim at the A sites from the top to bottom. Figure 3b and 3c are zoomed-in images from the boxes in the bright and dim regions in Fig. 3a, respectively. Clearly, we can see the corrugated oxygen octahedra tilting pattern in Fig. 3c. In contrast, Fig. 3b shows an apparently suppressed corrugated pattern, which is different from the split pattern since there is no elongation in oxygen columns. The insets of fast Fourier transform (FFT) images in Fig. 3b and 3c show correspondingly weak and strong superlattice diffraction spots, consistent with the degree of corrugations.

In HRTEM images taken under the ACI imaging mode, the intensity at the A-site column is dependent on the projected atomic number Z: light atomic columns are imaged as bright dots and heavy atomic columns are imaged as dim dots. Fig. 3d shows simulated HRTEM images with different ratios of Bi/Na at the A-site using simulation parameters described in Fig. S1. With the increase of Bi/Na ratio from 0.2/0.8 to 0.8/0.2, intensity at the A-site decreases. In the range of Bi/Na ratio from 0.2/0.8 to 0.5/0.5, there is no obvious intensity change at A-sites. In contrast, when Bi/Na ratio changes from 0.5/0.5 to 0.8/0.2, the A-site intensity becomes dimmer dramatically. Therefore, ACI-HRTEM imaging is not so sensitive to Na enrichment on the A-site, but it is very sensitive to Bi enrichment. In order to quantitatively measure the Bi/Na ratio on the A-site, we normalize the A-site intensity at each atomic column using two titanium columns above and below, i.e. $I_{n\,A} = I_A*2/(I_{Ti\ above}+I_{Ti\ below})$. The right column in Fig. 3d shows the normalized A-site intensity from simulated images. The average value of $I_{n\,A}$ in Fig. 3b is 1.0228±0.0182, indicating that Bi/Na ratio locates between 0.4/0.6 and 0.5/0.5. In contrast, $I_{n\,A}$ in Fig. 3c is 0.9544±0.0267, indicating that Bi/Na ratio is between 0.5/0.5 and 0.6/0.4. These results are consistent with the EDS measurements that the deviation of actual Bi/Na ratio from the stoichiometric value is around 10%.

As described above, Na-rich regions with bright A-site contrast in ACI images generally have less corrugation of oxygen octahedra while Bi-rich regions with dim A-sites contrast have more severe corrugation. To better visualize the correlation between A-site intensity and the degree of corrugation, we need to extract these two quantities separately from Fig. 4a. Since superlattice diffraction spots result only from the corrugation of oxygen octahedra, mapping of the degree of corrugation is obtained by acquiring an inverse FFT image (Fig. 4b) only using all these superlattice spots. The details of the process are described in Fig. S4 in the supplementary materials.

The degree of corrugation shown in Fig. 4b has roughly a negative correlation with Fig. 4a; that is, the top portion with stronger A-site intensity in Fig. 4a coincides with the weaker intensity of superlattice spots (less degree of corrugation) in Fig. 4b. Alternatively, a more accurate correlation can be established via directly measuring the A-site intensity and the degree of corrugation. To avoid any possible thickness change along the electron beam direction, A-site intensity is calibrated using the average intensity at Ti columns above and below an A-site. The degree of corrugation is measured using the separation width between above and below oxygen columns along $[001]_c$ direction. Figure 4c and 4d show the mapping of calibrated A-site intensity and the degree of corrugation. Unambiguously, the correlation is re-confirmed: Na-rich regions have less corrugation while Bi-rich regions are accompanied with stronger corrugation.

3.3 Nano-cluster-regions

Within the meso-domain which manifests chemical composition variation at tens of nanometer scale, we have further noticed many sharper contrasts at a much shorter length scale in HAADF images. A large collection angle (> 75 mrad) was used for acquiring the HAADF image in order to minimize diffraction contrast, and in this case, the HAADF intensity is approximately proportional to Z^2 (Z: atomic number). Many brighter (more Bi) or dimmer (more Na) regions are evident in Fig. 5a, which we termed “nano-cluster-regions”. It should be noted that such nano-cluster-regions are observed in corrugated/split orientation-domains as well as in Bi-/Na-rich meso-chemical-domains. As mentioned in the meso-chemical-domain section, the change of Bi/Na ratio would induce the variation in the degree of corrugation, which may remain valid in the nano-cluster-regions. As exemplified in Fig. 5b and 5c, the sudden change in the degree of corrugation occurs within two or three-unit cells. Unfortunately, it is difficult to directly correlate the nano-regions with the A-site contrast intensity, as the sample thickness is often larger than the nano-region dimension and overlapping effect does not allow us to discriminate unit-cell-level Bi/Na

ratio using the ACI mode. On the other hand, the intensity for a number of oxygen columns indicated by red arrows in Fig. 5b and 5c is significantly weaker. Weak intensity in the oxygen columns does reflect oxygen vacancy under ACI imaging conditions. In these regions, oxygen vacancies facilitate octahedral deformations and thus reduce corrugation, indicating a different mechanism for the nano-cluster-regions with oxygen vacancies clustering around Na cations.

4. Discussions

As a matter of fact, neither the inhomogeneity of A-site cations nor the variation in the degree of corrugation in BNT is surprising. Both Bi and Na are volatile species so they inevitably evaporate during the high temperature sintering process. The mobility of Bi and Na vacancies, even though much lower than that of oxygen vacancies, should allow them to migrate at elevated temperatures.[28] On the other hand, the complex phase transitions that take place during temperature decrease involve multiple phases with distinct tilting patterns, i.e. $Pm\bar{3}m$ ($a^0a^0a^0$), *P4bm* ($a^0a^0c^+$), *Pnma* ($a^-a^-c^+$), *R3c* ($a^-a^-a^-$), or *Cc* ($a^-a^-c^-$). Consequently, the tilting disorder is also likely to appear at room temperature.[8]

However, the impact of A-site non-stoichiometry on the tilting angle was rarely studied before. Jeong *et al*. found that the Na variation from +1% excess to -5% deficiency corresponds to a linear suppression of the $a^-a^-a^-$ tilting angle, while the Bi displays an opposite but much less significant trend.[29] This is apparently not in agreement with our present study that Na excess is associated with smaller degree of corrugation, if we assume only *R3c* phase is present. Recently, Cann and co-workers showed that 1% Na excess in $0.93(Bi_{1/2}Na_{1/2})TiO_3$–$0.07BaTiO_3$ solid solution almost doubles the volume fraction of the *P4bm* phase.[30] The addition of Ba into BNT essentially lowers the depolarization temperature and increases the *P4bm* phase fraction at room temperature.[31] So, in pure BNT where only a little residual of the high temperature *P4bm* phase persists to room temperature, the Na meso/nano-segregation is likely to stabilize the *P4bm* over

the *R3c* phase in the corresponding length scale. Since the *P4bm* phase features the in-phase oxygen octahedra tilting with respect to one of the four-fold axes, it would appear identical to the suppressed corrugated pattern when observed along the $<110>_c$ direction.

More importantly, the $6s^2$ lone pair electrons in Bi cation on A-site are known to be stereochemically active and are the primary driving force for the distortion of perovskite lattices.[32] In the meso-chemical-domain with a slight richness in Bi, it is plausible to have more severe lattice distortion. When it is in the *R3c* phase, a stronger corrugation is manifested.

Our present study provides a deeper insight for the dispersed dielectric response of BNT as a relaxor ferroelectrics by revealing the spatial variation of Bi and Na content at tens of nanometer scale as well as at unit-cell scale. This is a direct confirmation that BNT is an inhomogeneously disordered compound, which has implications on the electric dipole order as Bi-cation has higher charges than Na-cation. Consequently, the Bi-rich region (either at meso-scale or at nano-scale) is positively charged while the Na-rich region is negatively charged. Such paired regions can be considered as electric dipoles across unit cells up to even tens of nanometers. BNT, hence, possesses hierarchical electric dipoles.

5. Conclusions

In this work, a novel type of orientation-associated domain is identified in the BNT ceramic. Within the orientation-domain, meso-chemical-domains and nano-cluster-regions induced by composition variation or segregation are found. Taking advantage of the ACI mode in HRTEM, the correlation between the oxygen octahedra tilting pattern and the chemical non-stoichiometry is established. Our discovery encourages further explorations on the oxygen octahedra tilting engineering in designing new ferroelectric materials.

Acknowledgements

Work performed at the Center for Nanoscale Materials, a U.S. Department of Energy Office of Science User Facility, was supported by the U.S. DOE, Office of Basic Energy Sciences, under Contract No. DE-AC02-06CH11357. ZMF, XML, and XT acknowledge financial support from the U.S. National Science Foundation (NSF) through Grant DMR-1465254.

Conflict of Interest declaration:

The authors declare that they have NO affiliations with or involvement in any organization or entity with any financial interest in the subject matter or materials discussed in this manuscript.

References:

[1] Rödel J, Jo W, Seifert K T P, Anton E-M, Granzow T and Damjanovic D 2009 Perspective on the Development of Lead-free Piezoceramics *Journal of the American Ceramic Society* **92** 1153–77

[2] Guo Y, Liu Y, Withers R L, Brink F and Chen H 2011 Large Electric Field-Induced Strain and Antiferroelectric Behavior in (1-x)($Na_{0.5}Bi_{0.5}$)TiO_3-x$BaTiO_3$ Ceramics *Chem. Mater.* **23** 219–28

[3] Fan Z and Tan X 2019 Dual-stimuli in-situ TEM study on the nonergodic/ergodic crossover in the 0.75($Bi_{1/2}Na_{1/2}$)TiO_3–0.25$SrTiO_3$ relaxor *Appl. Phys. Lett.* **114** 212901

[4] Liu X and Tan X 2016 Giant Strains in Non-Textured ($Bi_{1/2}Na_{1/2}$)TiO_3-Based Lead-Free Ceramics *Advanced Materials* **28** 574–8

[5] Jones G O and Thomas P A 2002 Investigation of the structure and phase transitions in the novel A-site substituted distorted perovskite compound $Na_{0.5}Bi_{0.5}TiO_3$ *Acta Cryst B* **58** 168–78

[6] Gorfman S and Thomas P A 2010 Evidence for a non-rhombohedral average structure in the lead-free piezoelectric material $Na_{0.5}Bi_{0.5}TiO_3$ *J Appl Cryst* **43** 1409–14

[7] Ma C, Guo H and Tan X 2013 A New Phase Boundary in ($Bi_{1/2}Na_{1/2}$)TiO_3−$BaTiO_3$ Revealed via a Novel Method of Electron Diffraction Analysis *Advanced Functional Materials* **23** 5261–6

[8] Levin I and Reaney I 2012 Nano- and mesoscale structure of $Na_{1/2}Bi_{1/2}TiO_3$: A TEM Perspective *Advanced Functional Materials* **22**

[9] Beanland R and Thomas P A 2014 Symmetry and defects in rhombohedral single-crystalline $Na_{0.5}Bi_{0.5}TiO_3$ *Phys. Rev. B* **89** 174102

[10] Dorcet V and Trolliard G 2008 A transmission electron microscopy study of the A-site disordered perovskite $Na_{0.5}Bi_{0.5}TiO_3$ *Acta Materialia* **56** 1753–61

[11] Dorcet V, Trolliard G and Boullay P 2008 Reinvestigation of Phase Transitions in $Na_{0.5}Bi_{0.5}TiO_3$ by TEM. Part I: First Order Rhombohedral to Orthorhombic Phase Transition *Chem. Mater.* **20** 5061–73

[12] Trolliard G and Dorcet V 2008 Reinvestigation of Phase Transitions in $Na_{0.5}Bi_{0.5}TiO_3$ by TEM. Part II: Second Order Orthorhombic to Tetragonal Phase Transition *Chem. Mater.* **20** 5074–82

[13] Tang Y L, Zhu Y L, Ma X L, Borisevich A Y, Morozovska A N, Eliseev E A, Wang W Y, Wang Y J, Xu Y B, Zhang Z D and Pennycook S J 2015 Observation of a periodic array of flux-closure quadrants in strained ferroelectric $PbTiO_3$ films *Science* **348** 547–51

[14] Tang Y L, Zhu Y L, Wang Y J, Wang W Y, Xu Y B, Ren W J, Zhang Z D and Ma X L 2014 Atomic-scale mapping of dipole frustration at 90° charged domain walls in ferroelectric $PbTiO_3$ films *Sci Rep* **4** 4115

[15] Tang Y L, Zhu Y L, Liu Y, Wang Y J and Ma X L 2017 Giant linear strain gradient with extremely low elastic energy in a perovskite nanostructure array *Nat Commun* **8** 15994

[16] Han M J, Eliseev E A, Morozovska A N, Zhu Y L, Tang Y L, Wang Y J, Guo X W and Ma X L 2019 Mapping gradient-driven morphological phase transition at the conductive domain walls of strained multiferroic films *Phys. Rev. B* **100** 104109

[17] Han M J, Wang Y J, Ma D S, Zhu Y L, Tang Y L, Liu Y, Zhang N B, Ma J Y and Ma X L 2018 Coexistence of rhombohedral and orthorhombic phases in ultrathin BiFeO3 films driven by interfacial oxygen octahedral coupling *Acta Materialia* **145** 220–6

[18] Aso R, Kan D, Shimakawa Y and Kurata H 2013 Atomic level observation of octahedral distortions at the perovskite oxide heterointerface *Sci Rep* **3** 2214

[19] Li M, Zhang H, Cook S N, Li L, Kilner J A, Reaney I M and Sinclair D C 2015 Dramatic Influence of A-Site Nonstoichiometry on the Electrical Conductivity and Conduction Mechanisms in the Perovskite Oxide $Na_{0.5}Bi_{0.5}TiO_3$ *Chem. Mater.* **27** 629–34

[20] Gröting M, Hayn S and Albe K 2011 Chemical order and local structure of the lead-free relaxor ferroelectric $Na_{1/2}Bi_{1/2}TiO_3$ *Journal of Solid State Chemistry* **184** 2041–6

[21] Wen J G, Miller D J, Cook R E and Zaluzec N J 2014 Amplitude Contrast Imaging: High Resolution Electron Microscopy Using a Spherical and Chromatic Aberration Corrected TEM *Microscopy and Microanalysis* **20** 942–3

[22] Jia C-L, Urban K W, Alexe M, Hesse D and Vrejoiu I 2011 Direct Observation of Continuous Electric Dipole Rotation in Flux-Closure Domains in Ferroelectric $Pb(Zr,Ti)O_3$ *Science* **331** 1420–3

[23] Levin I, Reaney I M, Anton E-M, Jo W, Rödel J, Pokorny J, Schmitt L A, Kleebe H-J, Hinterstein M and Jones J L 2013 Local structure, pseudosymmetry, and phase transitions in $Na_{1/2}Bi_{1/2}TiO_3$--$K_{1/2}Bi_{1/2}TiO_3$ ceramics *Phys. Rev. B* **87** 024113

[24] Yoneda Y and Noguchi Y 2020 Nanoscale structural analysis of $Bi_{0.5}Na_{0.5}TiO_3$ *Jpn. J. Appl. Phys.* **59** SPPA01

[25] Ma T, Fan Z, Tan X and Zhou L 2019 Atomically resolved domain boundary structure in lead zirconate-based antiferroelectrics *Appl. Phys. Lett.* **115** 122902

[26] Urban K W, Jia C-L, Houben L, Lentzen M, Mi S-B and Tillmann K 2009 Negative spherical aberration ultrahigh-resolution imaging in corrected transmission electron microscopy *Philosophical Transactions of the Royal Society A: Mathematical, Physical and Engineering Sciences* **367** 3735–53

[27] Wang H, Wen J, Miller D J, Zhou Q, Chen M, Lee H N, Rabe K M and Wu X 2016 Stabilization of Highly Polar $BiFeO_3$-like Structure: A New Interface Design Route for Enhanced Ferroelectricity in Artificial Perovskite Superlattices *Phys. Rev. X* **6** 011027

[28] Tian C, Wang F, Ye X, Xie Y, Wang T, Tang Y, Sun D and Shi W 2014 Bipolar fatigue-resistant behavior in ternary $Bi_{0.5}Na_{0.5}TiO_3$–$BaTiO_3$–$SrTiO_3$ solid solutions *Scripta Materialia* **C** 25–8

[29] Jeong I-K, Sung Y S, Song T K, Kim M-H and Llobet A 2015 Structural evolution of bismuth sodium titanate induced by a-site non-stoichiometry: Neutron powder diffraction studies *Journal of the Korean Physical Society* **67** 1583–7

[30] Prasertpalichat S, Siritanon T, Nuntawong N and Cann D P 2019 Structural characterization of A-site nonstoichiometric $(1-x)Bi_{0.5}Na_{0.5}TiO_3$–$xBaTiO_3$ ceramics *J Mater Sci* **54** 1162–70

[31] Ma C, Tan X, Dul'kin E and Roth M 2010 Domain structure-dielectric property relationship in lead-free $(1-x)(Bi_{1/2}Na_{1/2})TiO_3$-$xBaTiO_3$ ceramics *Journal of Applied Physics* **108** 104105

[32] Seshadri R and Hill N A 2001 Visualizing the Role of Bi 6s "Lone Pairs" in the Off-Center Distortion in Ferromagnetic $BiMnO_3$ *Chem. Mater.* **13** 2892–9

[33] Benedek N A and Fennie C J 2011 Hybrid Improper Ferroelectricity: A Mechanism for Controllable Polarization-Magnetization Coupling *Phys. Rev. Lett.* **106** 107204

[34] Bousquet E, Dawber M, Stucki N, Lichtensteiger C, Hermet P, Gariglio S, Triscone J-M and Ghosez P 2008 Improper ferroelectricity in perovskite oxide artificial superlattices *Nature* **452** 732–6

[35] Liu X Q, Wu J W, Shi X X, Zhao H J, Zhou H Y, Qiu R H, Zhang W Q and Chen X M 2015 Hybrid improper ferroelectricity in Ruddlesden-Popper $Ca_3(Ti,Mn)_2O_7$ ceramics *Appl. Phys. Lett.* **106** 202903

[36] Wu X, Rabe K M and Vanderbilt D 2011 Interfacial enhancement of ferroelectricity in $CaTiO_3$/$BaTiO_3$ superlattices *Phys. Rev. B* **83** 020104

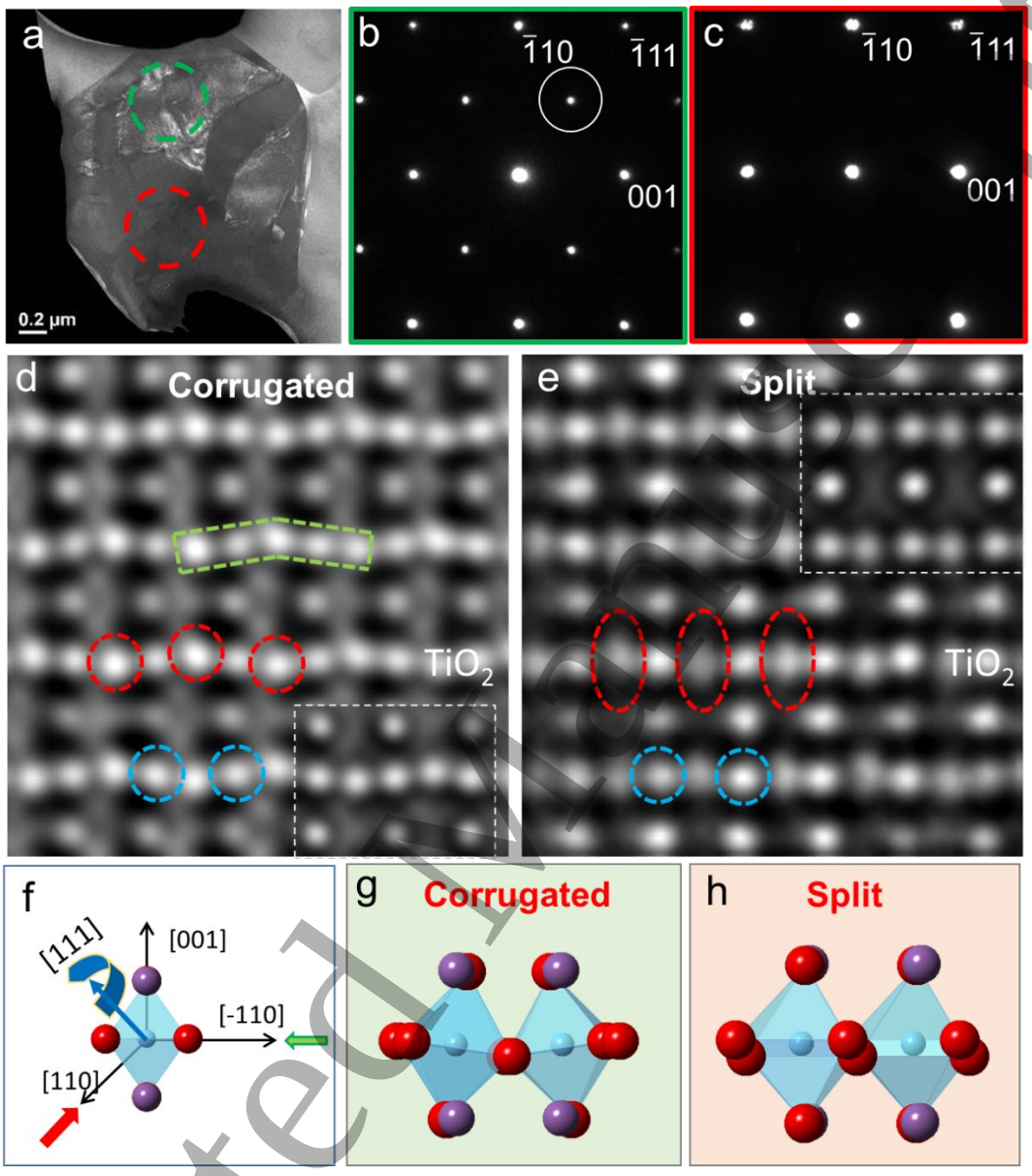

Fig. 1 Orientation-domains with different oxygen octahedral tilting patterns in a single grain of BNT. a) Dark-field TEM image using the circled diffraction spot ½[$\bar{1}$11] in b). Selected-area electron diffraction pattern in b) and c) are from green and red circled regions in a). Corresponding HRTEM images from green and red circled regions in a) showing d) corrugated and e) split features. Two insets are simulated HRTEM images with major simulation parameters as follow: Δf = -1 nm, C_s = 5 μm, t = 7 nm. f) Schematic diagram showing tilting of an oxygen octahedral about [$\bar{1}$11] direction. Viewing along [$\bar{1}$10] or [110] results in g) corrugated or h) split patterns, respectively.

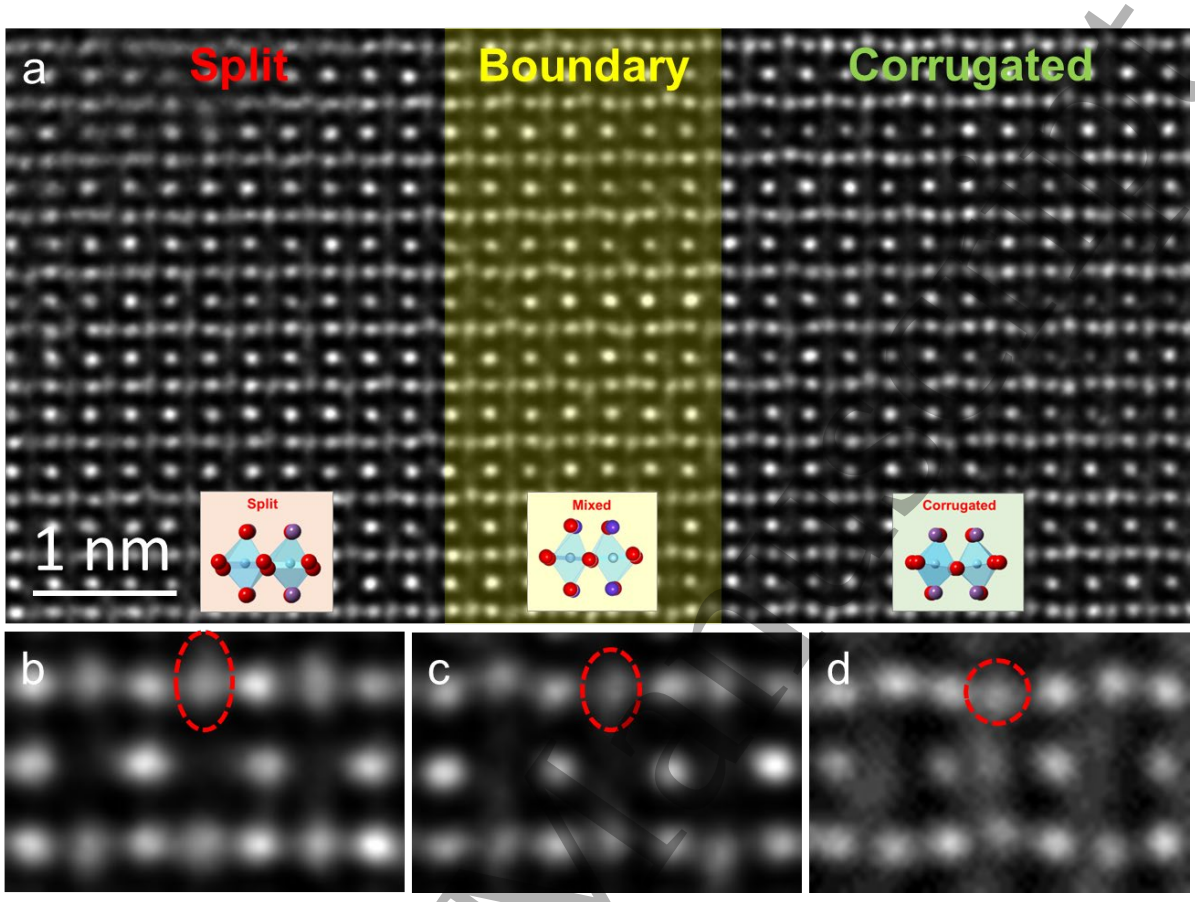

Fig. 2 a) HRTEM image showing a transition from "split" to "corrugated" pattern at orientation-domain boundaries. b), c), and d) are zoomed-in HRTEM images from split, boundary, and corrugated regions, respectively.

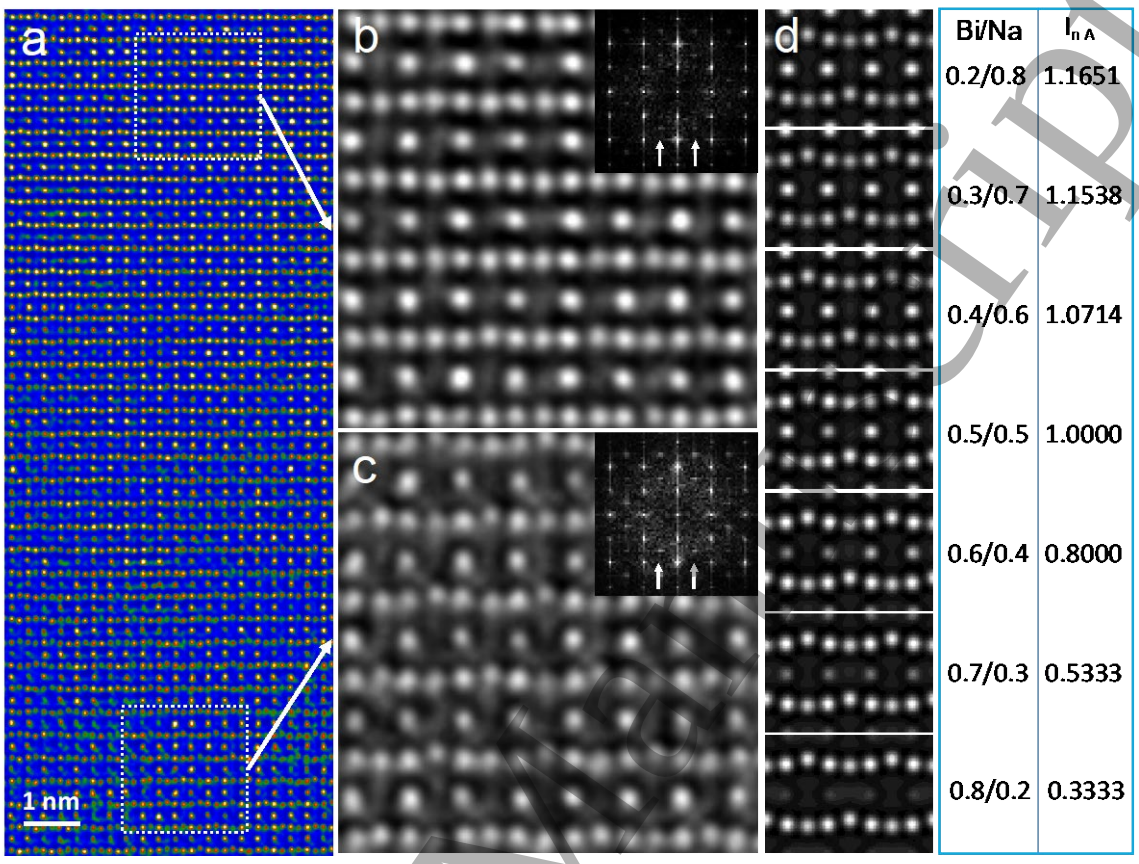

Fig. 3 ACI-HRTEM image of meso-chemical-domain associated with A-site composition. a) original amplitude-contrast HRTEM image. Note the top part has bright A-site intensity and the bottom part has dim A-site intensity. b) Zoomed-in image from the bright area shows less corrugation (corresponding to superlattice extra spots in the inserted FFT). c) Zoomed-in image from the dim area shows more corrugation (corresponding to strong superlattice spots in the inserted FFT). d) Simulated HRTEM images with different Bi/Na ratio at A-site.

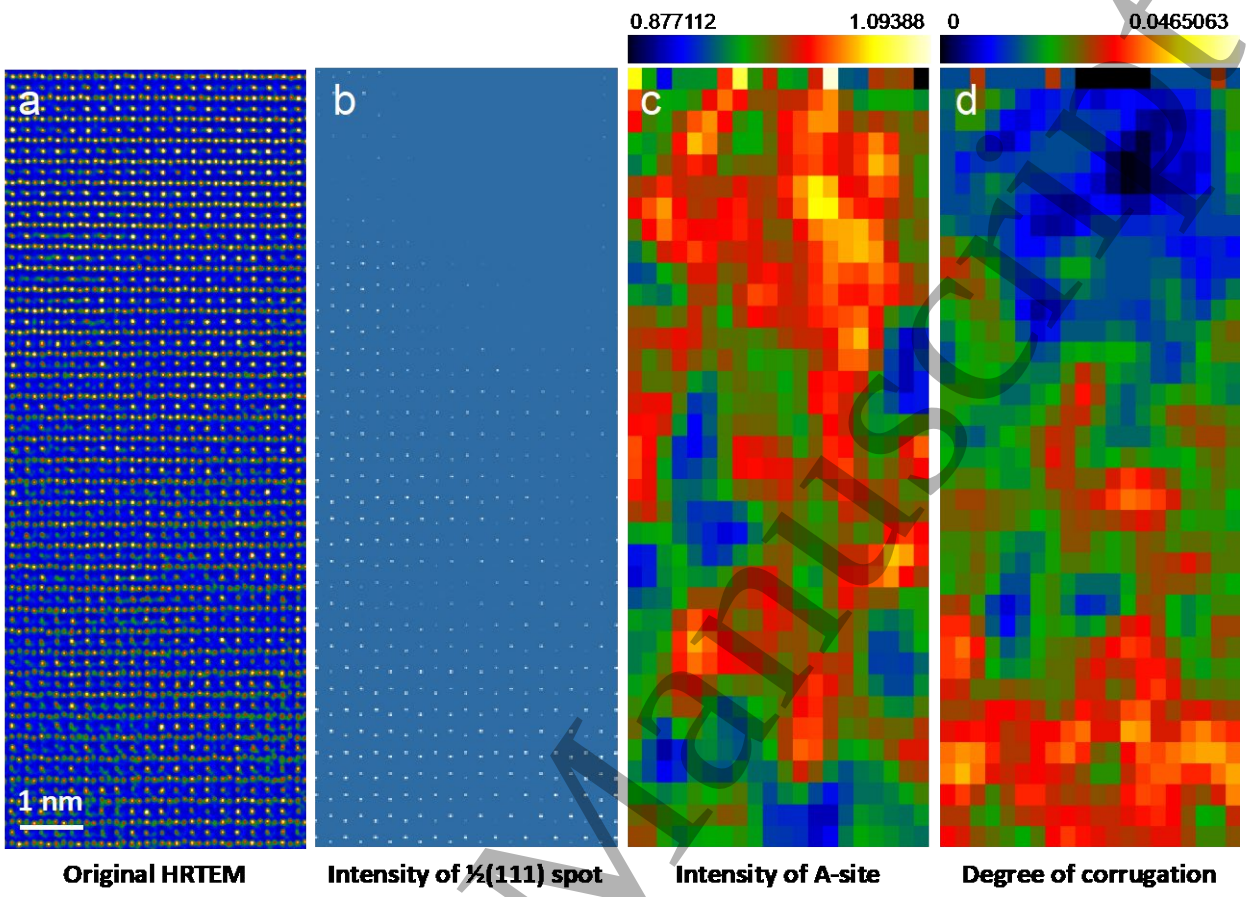

Fig. 4 Correlation between A-site intensity and degree of corrugation. a) original HRTEM image as shown in Fig. 3a. b) Inverse Fast-Fourier-Transform image using all extra diffraction spots. c) Direct mapping of calibrated A-site intensity from a). d) Degree of corrugation measured from the width of up and down oxygen columns from a).

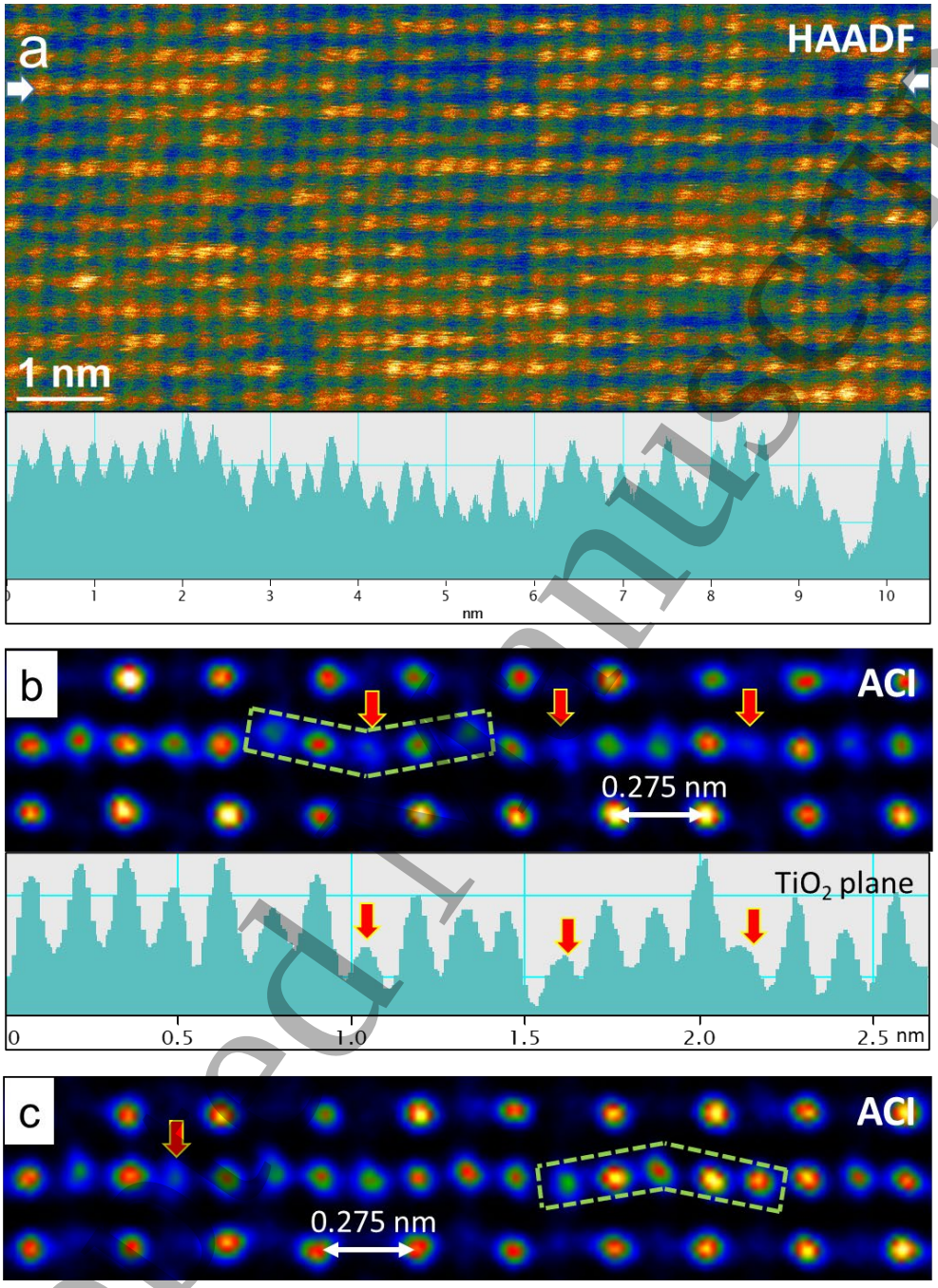

Fig. 5 a) HAADF image showing nano-cluster-regions associated with A-site nano-segregation. Dim (bright) regions correspond to Na-rich (Bi-rich), respectively. An intensity profile from the atomic row indicated by two white arrows is shown below. b) and c) HRTEM images under an amplitude-contrast image (ACI) mode show the isolated corrugation of oxygen octahedra at unit-cells scale. For a number of oxygen columns indicated by red arrows, the intensity is weaker, indicating oxygen vacancy. In these regions, reduced corrugations are also observed.